

Phonons and Lattice Dielectric Properties of Zirconia

Xinyuan Zhao and David Vanderbilt

Department of Physics and Astronomy, Rutgers University, Piscataway, NJ 08854-8019

(August 28, 2001)

We have performed a first-principles study of the structural and vibrational properties of the three low-pressure (cubic, tetragonal, and especially monoclinic) phases of ZrO_2 , with special attention to the computation of the zone-center phonon modes and related dielectric properties. The calculations have been carried out within the local-density approximation using ultrasoft pseudopotentials and a plane-wave basis. The fully relaxed structural parameters are found to be in excellent agreement with experimental data and with previous theoretical work. The total-energy calculations correctly reproduce the energetics of the ZrO_2 phases, and the calculated zone-center phonon frequencies yield good agreement with the infrared and Raman experimental frequencies in the monoclinic phase. The Born effective charge tensors are computed and, together with the mode eigenvectors, used to decompose the lattice dielectric susceptibility tensor into contributions arising from individual infrared-active phonon modes. This work has been partially motivated by the potential for ZrO_2 to replace SiO_2 as the gate-dielectric material in modern integrated-circuit technology.

PACS numbers: 77.22.-d, 61.66.-f, 63.20.-e, 77.84.Bw

I. INTRODUCTION

ZrO_2 , or zirconia, has a wide range of materials applications because of its high strength and stability at high temperature. A prospective application of particular current interest is its possible use to replace SiO_2 as the gate-dielectric material in metal-oxide-semiconductor (MOS) devices.

The use of SiO_2 as the gate dielectric, and in particular the quality of the Si/ SiO_2 interface, have been a foundation of modern integrated-circuit technology since its invention decades ago. Driven by the seemingly endless pressure for higher operation speed, smaller physical dimensions, and lower driving voltage, the gate dielectric thickness in integrated circuits has been rapidly reduced from the order of 1–2 μm in the early 1960s to the current value of about 2–3 nm. If SiO_2 is not replaced by another material, this would require the gate dielectric thickness to be reduced to less than 1 nm in the coming decade.¹ Such a reduction in gate oxide thickness, however, would impose several severe problems on the current Si/ SiO_2 semiconductor technology, including a high level of direct tunneling current, a large degree of dopant (boron) diffusion in the gate oxide, and reliability problems associated with nonuniformity of the very thin film. It has been demonstrated that the direct tunneling current grows exponentially as the thickness of the gate dielectric film decreases.^{2,3} For films thinner than 2 nm, the tunneling current could become as large as 1 A/cm², which would require a level of power dissipation that would be intolerable for most digital device applications.⁴ These fundamental problems are largely attributable to the inherently low dielectric constant of silicon dioxide ($\epsilon \simeq 3.5$), quite small in comparison with many other oxide dielectrics.

Several approaches have been proposed for overcoming

these fundamental challenges associated with the use of SiO_2 films. In particular, much recent effort has been focused on metal oxides having a larger dielectric constant than that of SiO_2 , since these might be used to provide physically thicker dielectric films that are equivalent to much thinner SiO_2 ones in terms of their capacitance, but exhibiting a greatly reduced leakage current. Some of the proposed candidates include Ta_2O_5 ,^{5,6} TiO_2 , ZrO_2 , Y_2O_3 , Al_2O_3 , and hafnium and zirconium silicate systems ($\text{Hf}_{1-x}\text{Si}_x\text{O}_2$ and $\text{Zr}_{1-x}\text{Si}_x\text{O}_2$).⁷ Among these candidates, ZrO_2 is a promising one because of its good dielectric properties ($\epsilon \sim 20$) and thermodynamic stability in contact with the Si substrate.

Zirconia is known to have three low-pressure structural phases. The system passes from the monoclinic ground state to a tetragonal phase, and then eventually to a cubic phase, with increasing temperature. The monoclinic phase (space group C_{2h}^5 or $P2_1/c$) is thermodynamically stable below 1400 K. Around 1400 K a transition occurs to the tetragonal structure (space group D_{4h}^{15} or $P4_2/nmc$), which is a slightly distorted version of the cubic structure and is stable up to 2570 K. Finally, the cubic phase (space group O_h^5 or $Fm\bar{3}m$) is thermodynamically stable between 2570 K and the melting temperature at 2980 K. This information is summarized in Table I, which also shows the coordination number of the Zr and O atoms for each of the three phases. In the monoclinic phase there are two nonequivalent oxygen sites with coordination numbers of 3 (O_1) and 4 (O_2), while all the Zr atoms are equivalent and have a coordination of 7.

Our purpose is to investigate the lattice contributions to the dielectric properties of these three ZrO_2 phases, especially the monoclinic phase. Because previous experimental and theoretical work indicates that the electronic contribution to the dielectric constant is rather small ($\epsilon_\infty \simeq 5$) and is neither strongly anisotropic nor

TABLE I. The three low-pressure phases of ZrO_2 . The last three columns give the coordination numbers of the Zr and O atoms. (Atoms O_1 and O_2 are equivalent in the cubic and tetragonal, but not in the monoclinic, structures.)

Phase	Space group	T (K)	Coordination		
			Zr	O_1	O_2
Cubic	$Fm\bar{3}m$	2570 - 2980	8	4	4
Tetragonal	$P4_2/nmc$	1400 - 2570	8	4	4
Monoclinic	$P2_1/c$	<1400	7	3	4

strongly dependent on structural phase,^{8–12} and because ϵ_∞ is best calculated by specialized linear-response techniques, we have not calculated it here. Instead, we focus on the lattice contributions to the dielectric response because, as we shall see, these are much larger, more anisotropic, and more sensitive to the lattice structure.

In order to achieve this, the Born effective charge tensors and the force-constant matrices are calculated for the three ZrO_2 phases using density-functional theory. We first check that our relaxed structural parameters and energy differences between phases are consistent with previous theoretical^{13–20} and experimental work.^{21,22} The Born effective charge tensors are then computed from finite differences of polarizations as various sublattice displacements are imposed, with the polarizations computed using the Berry-phase method.²³ The force constants are obtained in a similar way from finite differences of forces. Reasonable agreement is found between the calculated frequencies and the measured spectra for both IR-active and Raman-active modes,^{9,24–27} although possible reassignments are proposed for certain modes based on the results of our calculations. Finally, our theoretical information is combined to predict the lattice contributions to the bulk dielectric tensor. We thus clarify the dependence of the dielectric response on crystal phase, orientation, and lattice dynamical properties. In particular, we find that the lattice dielectric tensors in the tetragonal and monoclinic phases are strongly anisotropic. We also find that the monoclinic phase has the smallest orientationally-averaged dielectric constant of the three phases, owing to the fact that the mode effective charges associated with the lowest-frequency modes are rather weak.

The paper is organized as follows. In Sec. II we briefly describe the technical aspects of our first-principles calculations. Sec. III presents the results, including the structural relaxations, the Born effective charge tensors, the phonon normal modes, and the lattice contributions to the dielectric tensors. Sec. IV concludes the paper.

II. DETAILS OF FIRST-PRINCIPLES CALCULATIONS

The calculations are carried out within a plane-wave pseudopotential implementation of density-functional

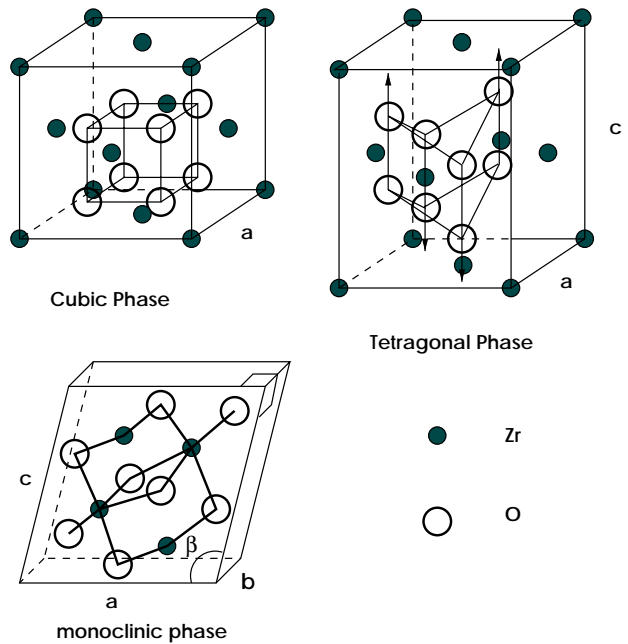


FIG. 1. Structures of the three ZrO_2 phases. The Zr–O bonds are only shown in the monoclinic structure. For the tetragonal phase, the arrows indicate the distortion of oxygen pairs relative to the cubic structure.

theory (DFT) in the local-density approximation (LDA) using Ceperley-Alder exchange-correlation.^{28,29} The use of Vanderbilt ultrasoft pseudopotentials³⁰ allows a highly accurate calculation to be achieved with a low energy cut-off, which is chosen to be 25 Ry in this work. The 4s and 4p semicore shells are included in the valence for Zr, and the 2s and 2p shells are included in the valence for O. A conjugate-gradient algorithm is used to compute the total energies and forces. For each of the three ZrO_2 phases, a unit cell containing 12 atoms (4 Zr and 8 O atoms) is used in our calculations. Although we thus use an unnecessarily large cell for the cubic and tetragonal phases, this approach has the advantage that the three zirconia phases can be studied in a completely parallel fashion.

A $4 \times 4 \times 4$ Monkhorst-Pack³¹ k-point mesh is found to provide sufficient precision in the calculations of total energies and forces. In order to calculate Born effective charges and force-constant matrices, each atomic sublattice in turn is displaced in each Cartesian direction by $\pm 0.2\%$ in lattice units, and the Berry-phase polarization²³ and Hellmann-Feynman forces are computed. To be specific, a $4 \times 4 \times 20$ k-point sampling over the Brillouin zone was used in the Berry-phase polarization calculations, and we have confirmed that good convergence was achieved for the three ZrO_2 phases with such k-point sampling. The Born effective charge tensors and force-constant matrices are then constructed by finite differences from the results of these calculations.

III. RESULTS

A. Atomic Structures of ZrO₂ Phases

The three crystal structures of ZrO₂ are shown in Fig. 1. Cubic zirconia takes the fluorite (CaF₂) structure, in which the Zr atoms are in a face-centered cubic structure and the oxygen atoms occupy the tetrahedral interstitial sites associated with this fcc lattice. The structure of tetragonal zirconia can be regarded as a distortion of the cubic structure obtained by displacing alternating pairs of oxygen atoms up and down by an amount Δz along the z direction, as shown in the figure. This doubles the primitive cell from three to six atoms and is accompanied by a tetragonal strain. The structure can be specified by the two lattice parameters a and c and a dimensionless ratio $d_z = \Delta z/c$. Cubic zirconia can be considered as a special case of the tetragonal structure with $d_z = 0$ and $c/a = 1$ (if the primitive cell is used for tetragonal phase, $c/a = \sqrt{2}$).

Monoclinic zirconia has a lower symmetry and a more complex geometric structure with a 12-atom primitive cell. The lattice parameters are a , b , c , and β (the non-orthogonal angle between \mathbf{a} and \mathbf{c}) as shown in Fig. 1. The atomic coordinates in Wyckoff (lattice-vector) notation are $\pm(x, y, z)$ and $\pm(-x, y + 1/2, 1/2 - z)$, with parameters x , y and z specified for each of three kinds of atoms: Zr, O₁, and O₂. Note that there are two non-equivalent oxygen sites: atoms of type O₁ are 3-fold coordinated, while O₂ are 4-fold coordinated. All Zr atoms are equivalent and are 7-fold coordinated. Thus, four lattice-vector parameters and nine internal parameters are needed to specify the structure fully.

Tabulated in Table II are the relaxed structural parameters for the three phases of ZrO₂ as computed within our energy minimization procedure, as well as results of previous theoretical and experimental work for comparison. The experimental parameters given in the last column were used as the starting point for our DFT-LDA structural relaxations. It can readily be seen that there is excellent agreement between our results and previous theory and experiment. The volumes are all slightly underestimated, by 2-3%, as is typical of LDA calculations. The largest discrepancy is for $d_z = \Delta z/c$, the internal coordinate in the tetragonal phase; our value is $\sim 30\%$ smaller than the experimental value, but it is very closed to the results of the previous pseudopotential calculation. (The discrepancy with experiment should not be taken too seriously, in view of the fact that the theory is a zero-temperature one.) The very close (usually $< 1\%$) agreement with the previous pseudopotential results of Ref. 16 provides a good confirmation of the reliability of our calculations.

Fig. 2 illustrates the relaxed monoclinic structure, and Table III lists the calculated bond lengths and bond angles for the O-Zr bonds. Bond lengths taken from Ref. 32 are also listed for comparison. As can be seen in the fig-

TABLE II. Structural parameters obtained for three ZrO₂ phases from present theory, compared with previous pseudopotential (PP) and linear augmented plane-wave (FLAPW) calculations and with experiment. Lattice parameters a , b , c and volume per formula unit V are in atomic units; monoclinic angle β is in degrees; and internal coordinates d_z , x , y and z are dimensionless.

	This work	PP ^a	FLAPW ^b	Expt. ^c
Cubic				
V	215.612	215.31	217.79	222.48
a	9.5187	9.514	9.551	9.619
Tetragonal				
V	217.698	218.69	218.77	222.96
a	9.5051	9.523	9.541	9.543
c	9.6383	9.646	9.613	9.793
d_z	0.0418	0.0423	0.029	0.0574
Monoclinic				
V	231.822	230.51		237.71
a	9.6532	9.611		9.734
b	9.7690	9.841		9.849
c	9.9621	9.876		10.048
β	99.21	99.21		99.23
x_{Zr}	0.2769	0.2779		0.2754
y_{Zr}	0.0422	0.0418		0.0395
z_{Zr}	0.2097	0.2099		0.2083
x_{O_1}	0.0689	0.0766		0.0700
y_{O_1}	0.3333	0.3488		0.3317
z_{O_1}	0.3445	0.3311		0.3447
x_{O_2}	0.4495	0.4471		0.4496
y_{O_2}	0.7573	0.7588		0.7569
z_{O_2}	0.4798	0.4830		0.4792

^aRef. 16.

^bRef. 20.

^cRef. 13.

TABLE III. O-Zr bond lengths and Zr-O-Zr bond angles in monoclinic zirconia (in Å and degrees respectively). Values in parentheses are from Ref. 32 for comparison.

O₁-Zr bond lengths and angles				
d_1	2.035	(2.051)	θ_{12}	138.6
d_2	2.051	(2.057)	θ_{13}	106.3
d_3	2.144	(2.151)	θ_{23}	105.0
O₂-Zr bond lengths and angles				
d_1	2.138	(2.163)	θ_{12}	108.6
d_2	2.229	(2.220)	θ_{13}	106.0
d_3	2.153	(2.189)	θ_{14}	133.0
d_4	2.233	(2.285)	θ_{23}	102.0
			θ_{24}	100.6
			θ_{34}	103.6

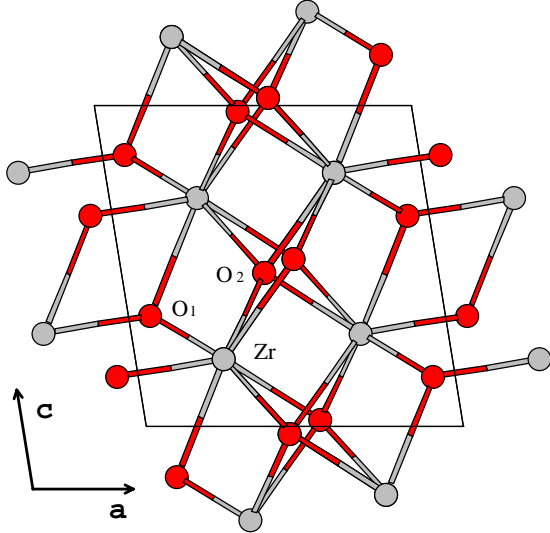


FIG. 2. Relaxed lattice structure of monoclinic ZrO_2 ; unit cell is outlined. Light and dark circles stand for the Zr and O atoms, respectively. A 3-fold coordinated oxygen atom (O_1) is bonded to the nearest neighboring Zr atoms in an almost planar configuration, while a 4-fold oxygen atom (O_2) forms a distorted tetrahedron with the Zr neighbors.

ure, a three-fold coordinated oxygen atom (O_1) is bonded to the three nearest-neighbor Zr atoms in an almost planar configuration, as can be verified by noting that the sum of the three bond angles is about 350° . A second four-fold oxygen atom (O_2) forms a distorted tetrahedron with its four nearest Zr neighbors, the degree of distortion being evident from the lengths and angles in the table. The presence of these two distinct oxygen atoms with utterly different environments suggests that their contributions to the dielectric properties of the material may be quite different. We shall see how this is manifest as a difference of the Born effective charge tensors for O_1 and O_2 in the next subsection.

Our total-energy calculations have correctly reproduced the energetics of the three ZrO_2 phases. The differences of total energies per formula unit for the monoclinic and tetragonal phases, relative to the cubic phase, are 0.044 eV and 0.089 eV respectively, to be compared with 0.045 eV and 0.102 eV from previous calculation,¹⁶ and 0.057 eV and 0.120 eV from one experiment.³³

B. Born Effective Charge Tensors

The Born effective charge tensor quantifies the macroscopic electric response of a crystal to internal displacements of its atoms. We begin with a calculation of the bulk polarization \mathbf{P} , using the Berry-phase polarization method to compute the electronic contribution, as formulated in Ref. 23. \mathbf{Z}_i^* , the Born effective charge tensor for the i -th atom in the unit cell, is defined via

TABLE IV. Born effective charges for three phases of ZrO_2 . In the cubic phase, the \mathbf{Z}^* tensors are diagonal and isotropic. In the tetragonal phase, the \mathbf{Z}^* tensors are diagonal in an $x'-y'-z$ frame rotated 45° about \hat{z} from the Cartesian frame; Z_j^* ($j=1,2,3$) are $Z_{x'x'}$, $Z_{y'y'}$, and Z_{zz} , respectively. In the monoclinic phase, Z_j^* is the j 'th eigenvalue of the symmetric part of the \mathbf{Z}^* tensor.

Phase	Atom	Z_1^*	Z_2^*	Z_3^*
Cubic	Zr	5.72	5.72	5.72
	O	-2.86	-2.86	-2.86
Tetragonal	Zr	5.75	5.75	5.09
	O_1	-3.53	-2.22	-2.53
	O_2	-2.22	-3.53	-2.56
Monoclinic	Zr	4.73	5.42	5.85
	O_1	-4.26	-2.64	-1.19
	O_2	-3.20	-2.52	-2.26

$$\Delta\mathbf{P} = \frac{e}{V} \sum_{i=1}^N \mathbf{Z}_i^* \cdot \Delta\mathbf{u}_i \quad (1)$$

where V is the volume of the unit cell, $\Delta\mathbf{u}_i$ is the displacement of the i -th atom in the unit cell, and $\Delta\mathbf{P}$ is the induced change in bulk polarization resulting from this displacement. Using Eq. (1), \mathbf{Z}^* can be computed from finite differences of \mathbf{P} under small but finite distortions.³⁴

In the Berry-phase polarization scheme, one samples the Brillouin zone by a set of strings of k -points set up parallel to some chosen reciprocal lattice vector, thereby computing the electronic polarization along that direction. For cubic and tetragonal ZrO_2 , this is relatively straightforward since the reciprocal lattice vectors are all mutually perpendicular. For monoclinic ZrO_2 , however, one has to transform the polarization to Cartesian coordinates after first computing it in lattice coordinates.

Our results for the dynamical effective charges of the three phases are presented in Table IV. In the cubic phase, symmetry requires that the Born effective charge tensor should be isotropic ($Z_{ij}^* = Z^* \delta_{ij}$) on each atom, and that $Z^*(\text{O}_1) = Z^*(\text{O}_2)$; the neutrality sum rule requires that $Z^*(\text{Zr}) = -2 Z^*(\text{O})$. The values given in Table IV can be seen to be in excellent agreement with the corresponding values of $Z^*(\text{Zr}) = 5.75$ and $Z^*(\text{O}) = -2.86$ reported in Ref. 8.

In the tetragonal phase, $\mathbf{Z}^*(\text{Zr})$ is diagonal in the Cartesian frame with $Z_{xx}^* = Z_{yy}^* \neq Z_{zz}^*$. The diagonal elements of $\mathbf{Z}^*(\text{O})$ have the same form, but the shifting of oxygen atom pairs creates two different configurations for oxygen atoms (denoted O_1 and O_2) and introduces off-diagonal xy elements. Specifically, $Z_{xy}^*(\text{O}_1) = Z_{yx}^*(\text{O}_1) = -Z_{xy}^*(\text{O}_2) = -Z_{yx}^*(\text{O}_2)$. Thus, it is more natural to refer to a reference frame that has been rotated 45° about the \hat{z} axis; in this frame the $\mathbf{Z}^*(\text{O})$ become diagonal. This symmetry analysis is confirmed in our calculations, as can be seen from Table IV. We have recently become aware of the independent work of Ref. 12, which also reports values for the \mathbf{Z}^* tensors in the

tetragonal phase of ZrO_2 . These authors find $Z_{xx}^*=5.74$ and $Z_{zz}^*=5.15$ for Zr, and $Z_{x'x'}^*=-3.52$, $Z_{y'y'}^*=-2.49$ and $Z_{zz}^*=-2.57$ for oxygens. Evidently there is again very good agreement between our results and those of previous theory.

In the monoclinic phase, the Born effective charge tensors are more complicated because of the complexity of the lattice structure. The two oxygen sites are now non-equivalent, and the crystal structure should be regarded as composed of three kinds of atoms, namely, Zr, O_1 , and O_2 . Each kind of atom appears four times in the unit cell, once at a “representative” Wyckoff position (x, y, z) , and then also at partner positions $(-x, -y, -z)$, $(-x, 0.5 + y, 0.5 - z)$ and $(x, 0.5 - y, 0.5 + z)$ given by action of the space-group operations E , I , $\{C_2^y | 0, 0.5, 0.5\}$ and $\{M_y | 0, 0.5, 0.5\}$. Thus, all three kinds of atoms have equally low symmetry, and their resulting \mathbf{Z}^* tensors are neither diagonal nor symmetric. Specifically, for these representative atoms we find

$$\mathbf{Z}^*(\text{Zr}) = \begin{pmatrix} 5.471 & -0.432 & 0.180 \\ -0.155 & 5.608 & 0.152 \\ 0.197 & 0.376 & 4.952 \end{pmatrix}$$

$$\mathbf{Z}^*(\text{O}_1) = \begin{pmatrix} -3.019 & 1.172 & -0.199 \\ 1.449 & -2.755 & -0.695 \\ -0.191 & -0.684 & -2.321 \end{pmatrix}$$

$$\mathbf{Z}^*(\text{O}_2) = \begin{pmatrix} -2.461 & 0.171 & 0.018 \\ 0.238 & -2.850 & 0.372 \\ -0.019 & 0.413 & -2.657 \end{pmatrix}$$

We have confirmed that our computed effective-charge tensors for the other atoms obey the relations expected by symmetry, namely, that the \mathbf{Z}^* tensors should be identical for partners at $(-x, -y, -z)$, and that the off-diagonal xy , yx , yz , and zy matrix elements should change sign for the partners at $(-x, 0.5 + y, 0.5 - z)$ and $(x, 0.5 - y, 0.5 + z)$. In Table IV we report the eigenvalues of the symmetric part of the effective-charge tensors.

It is obvious from Table IV that the Z^* values are quite different from the nominal ionic valences (+4 for Zr and -2 for O). Except for the value of -1.19, all other magnitudes are greater than their nominal valences. The anomalously large Z^* values indicate that there is a strong dynamic charge transfer along the Zr–O bond as the bond length varies, indicating a mixed ionic-covalent nature of the Zr–O bond. Such an anomaly reflects the relatively delocalized structure of the electronic charge distributions, and is quite common in other weakly ionic oxides such as the ferroelectric perovskites.³⁵

As discussed in Sec. III A, the oxygen atom of type O_1 is bonded to three nearest-neighbor Zr atoms in an almost planar configuration. One might then expect that the largest dynamical charge transfer would occur for motions of the O atom in this plane, with a smaller magnitude of Z^* for motion perpendicular to this plane. To

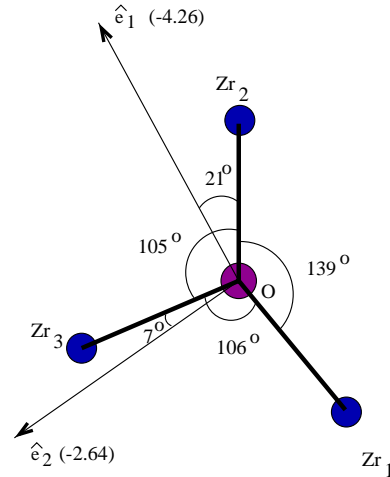


FIG. 3. Environment of three-fold coordinated O_1 atom in the monoclinic phase. The three Zr–O bonds lie approximately in a plane. \hat{e}_1 and \hat{e}_2 are the two principal axes associated with the eigenvalues -4.26 and -2.64 of the symmetric part of the Z^* tensor, respectively.

check this, we computed the eigenvectors that result from diagonalizing the symmetric part of the Born charge tensor of the O_1 atom, corresponding to the eigenvalues in the penultimate row of Table IV. Sure enough, the principle axis \hat{e}_3 associated with the eigenvalue $Z_3^*=-1.19$ of smallest magnitude points almost directly normal to the plane of the neighbors (making angles of 85° , 91.2° and 93.9° to the three O–Zr bonds). The other two principal axes lie essentially in the plane of the neighbors, as shown in Fig. 3. Moreover, the principal axis \hat{e}_1 connected with the eigenvalue $Z_1^*=-4.26$ of largest magnitude is nearly parallel to the bond to the closest neighbor Zr_1 . It can also be seen that the vector \hat{e}_2 connected with the intermediate eigenvalue is very nearly aligned with the O_1 – Zr_3 bond. Not surprisingly in view of its more tetrahedral coordination, the Z^* tensor for atom O_2 is more isotropic, as indicated by the smaller spread of the eigenvalues in the last line of Table IV.

C. Phonons

The frequencies of phonons at Γ , the center of the Brillouin zone, are calculated for the cubic, tetragonal and monoclinic phases. For each phase, we first calculate the force-constant matrix

$$\Phi_{ij}^{\alpha\beta} = -\frac{\partial F_i^\alpha}{\partial u_j^\beta} \simeq -\frac{\Delta F_i^\alpha}{\Delta u_j^\beta} \quad (2)$$

obtained by calculating all the Hellmann-Feynman forces (F_i^α) caused by displacing each ion in each possible direction (u_j^β) in turn. (Here Greek indices label the Cartesian coordinates, and i and j run over all the atoms in

TABLE V. Frequencies (in cm^{-1}) of IR-active phonon modes for ZrO_2 phases. For monoclinic ZrO_2 , a possible re-assignment is proposed. Notation ‘sh’ stands for ‘shoulder’ as in the original reference. Modes labeled ‘weak’ have very small intensity. Ref. 37 is a previous theoretical work.

Cubic	This work			
1	258 (T_{1u})			
Tetrag.	This work	Expt. 38	Expt. 39	Ref. 37
1	154 (E_u)	140	164	146
2	437 (E_u)	550	467	466
3	334 (A_{2u})	320	339	274
Mono.	This work	Expt. 9	Expt. 25	Expt. 27
		104		
1	181 (B_u) ^{weak}	180		
		192		
2	224 (A_u)	235	220	224
3	242 (A_u)			
4	253 (B_u)	270	250	257
5	305 (A_u)			
6	319 (B_u)			324 ^{sh} (?)
7	347 (A_u)			
8	355 (B_u)	360	330	351
		375	370	376
9	401 (A_u)			
10	414 (B_u)	415	420	417
		445	440	453 ^{sh}
11	478 (A_u)			
12	483 (B_u)	515	520	511
13	571 (A_u)	620	600	588
14	634 (A_u) ^{weak}			687 (?)
				725 (?)
15	711 (B_u)	740	740	789

the unit cell.) In practice, we take steps Δu that are 0.2% in lattice units, average over steps in positive and negative directions, and the resulting Φ matrix is symmetrized to clean up numerical errors. The dynamical matrix $D_{ij}^{\alpha\beta} = (M_i M_j)^{-1/2} \Phi_{ij}^{\alpha\beta}$ is then diagonalized to obtain the eigenvalues ω^2 . Once again, we will mainly focus on the monoclinic phase, and briefly summarize the results for the cubic and tetragonal phases.

The low-temperature phase of ZrO_2 is monoclinic, with space group $P2_1/c$. The little group at Γ is the point group C_{2h} consisting of operations E , I , C_2^y , and M_y . The character table of this point group indicates that there are four symmetry classes and thus four irreducible representations, each of which is one-dimensional. A standard group-theoretical analysis indicates that the modes at the Γ point can be decomposed as

$$\Gamma_{\text{vib}}^{\text{mono}} = 9A_g \oplus 9A_u \oplus 9B_g \oplus 9B_u \quad (3)$$

(see also Ref. 24). Of the 36 modes, 18 modes ($9A_g + 9B_g$) are Raman-active and 15 modes ($8A_u + 7B_u$) are infrared-active, the remaining three modes being the zero-frequency translational modes. Only the 15 infrared-active modes contribute to the lattice dielectric

tensor, as discussed in the next subsection. Similarly, for the tetragonal ZrO_2 phase,

$$\Gamma_{\text{vib}}^{\text{tetra}} = 1A_{1g} \oplus 2A_{2u} \oplus 3E_g \oplus 3E_u \oplus B_{2u} \oplus 2B_{1g}, \quad (4)$$

where the E_u and E_g representations are two-dimensional while all other modes are one-dimensional. One A_{2u} mode and one E_u pair are acoustic, leaving one IR-active A_{2u} and two IR-active E_u pairs; A_{1g} , B_{1g} and E_g are Raman-active, and B_{2u} is silent (see also Ref. 36). For the cubic phase one finds

$$\Gamma_{\text{vib}}^{\text{cubic}} = 2T_{1u} \oplus T_{1g} \quad (5)$$

where both T_{1u} and T_{1g} representations are three-dimensional. One of the T_{1u} triplets is translational, leaving one IR-active T_{1u} triplet.

Table V lists our calculated IR-active phonon frequencies in comparison with available theoretical³⁷ and experimental values.^{9,25,27,38,39} In some cases, possible re-assignments are suggested. The overall agreement is very good; we obtain all the major features of the experimental infrared spectra. In order to facilitate comparison with experiment, the oscillator strengths of the infrared-active modes (namely ϵ_λ , see Eqs. (8-9) of the Sec. III D) are calculated and plotted versus frequency in Fig. 4. The horizontal axis is reversed for comparison with experimental spectra such as that of Fig. 2 of Ref. 25. The solid and dashed lines indicate A_u and B_u modes, respectively. The two modes at 181 cm^{-1} and 634 cm^{-1} are very weak, so that it is not surprising that they were not observed in most experiments. The mode at 242 cm^{-1} is buried by the modes at 253 cm^{-1} and 224 cm^{-1} , while the mode at 305 cm^{-1} is similarly shadowed by the strongest mode at 319 cm^{-1} . Because the pairs of modes at $347/355 \text{ cm}^{-1}$, $401/414 \text{ cm}^{-1}$ and $478/483 \text{ cm}^{-1}$ are very close and of comparable strength, we think that they might be observed as single modes in the experiments.

The calculated Raman-active phonon mode frequencies for the monoclinic structure are summarized in Table VI. The overall pattern of the calculated Raman-active spectrum agrees quite well with the experimental results, but we again suggest possible reassignments of some of the modes. Specifically, we obtained one Raman-active mode at 180 cm^{-1} that was not observed in either experiment. We agree with Carlone²⁶ in excluding the mode at 355 cm^{-1} suggested in Ref. 24, and in interpreting the feature at 780 cm^{-1} as a first-order and not a second-order one.²⁴ On the other hand, our calculations do not give any frequency close to 705 cm^{-1} as observed by Carlone.²⁶ The mode at 317 cm^{-1} obtained in our calculation is observed somewhat ambiguously in one experiment²⁴ but not in the other.²⁶ The reason why we assigned the highest calculated mode at 748 cm^{-1} as shown in Table VI is that the corresponding Raman spectra at 15 K indicated this mode at 745 cm^{-1} .²⁶

The overall good correspondence between our results and the experimental data for both infrared and Raman-active modes therefore tends to justify our phonon analysis, suggesting that we are now on firm ground to proceed

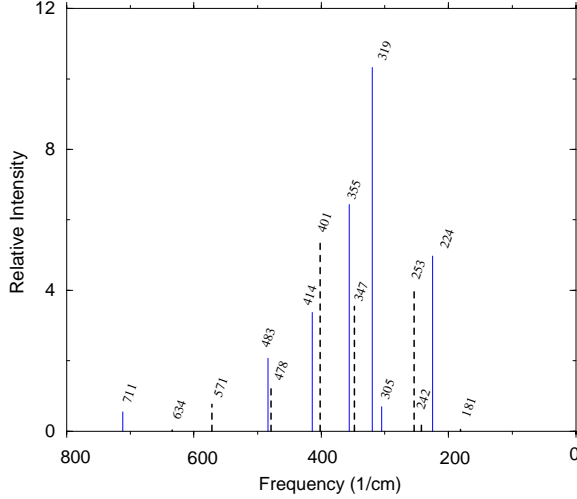


FIG. 4. Calculated spectrum of IR-active modes, in which orientationally-averaged intensity (ϵ_λ of Eq. (9)) is plotted vs. mode frequency in cm^{-1} (see labels on modes). Solid and dashed lines indicate A_u and B_u IR-active modes respectively.

to the calculation of the lattice contributions to the dielectric tensors for the ZrO_2 phases.

D. Lattice Dielectric Tensors

In this section, we present our calculations of the lattice contributions to the static dielectric tensor (ϵ_0), which can be separated into contributions arising from purely electronic screening (ϵ_∞) and IR-active phonon modes according to⁴⁰

$$\epsilon_{\alpha\beta}^0 = \epsilon_{\alpha\beta}^\infty + \frac{4\pi e^2}{M_0 V} \sum_\lambda \frac{\tilde{Z}_{\lambda\alpha}^* \tilde{Z}_{\lambda\beta}^*}{\omega_\lambda^2}. \quad (6)$$

Here α and β label Cartesian coordinates, e is the electron charge, M_0 is a reference mass that we take for convenience to be 1 amu, ω_λ is the frequency of the λ -th IR-active phonon normal mode, and V is the volume of the three-atom, six-atom, or 12-atom unit cell for cubic, tetragonal, or monoclinic cases, respectively. The mode effective charge tensors $\tilde{Z}_{\lambda\alpha}^*$ are given by

$$\tilde{Z}_{\lambda\alpha}^* = \sum_{i\beta} Z_{i,\alpha\beta}^* \left(\frac{M_0}{M_i} \right)^{1/2} \xi_{i,\lambda\beta} \quad (7)$$

where $\xi_{i,\lambda\beta}$, the eigendisplacement of atom i in phonon mode λ , is normalized according to $\sum_{i\alpha} \xi_{i,\lambda\alpha} \xi_{i,\lambda'\alpha} = \delta_{\lambda\lambda'}$. It is also convenient to write

$$\text{Tr}[\epsilon^0] = \text{Tr}[\epsilon^\infty] + \sum_\lambda \epsilon_\lambda \quad (8)$$

where

TABLE VI. Frequencies (cm^{-1}) of Raman-active phonon modes (A_g and B_g) in monoclinic ZrO_2 . Experimental data are measured at 300 K. The assignment connecting the two sets of experimental results is adopted from Ref. 26. We also adopt the notations introduced by the authors of Ref. 24: ‘ambig’ for ‘observed ambiguously,’ ‘tetra’ for ‘tetragonal phase,’ ‘sugg’ for ‘unobserved suggested,’ and ‘2nd’ for ‘second order.’

Mode	This Work	Mode	Expt. 26	Mode	Expt. 24
				1	92 ^{ambig}
1	103 (A_g)	1	99	2	101
					148 ^{tetra}
2	175 (B_g)	2	177	3	177
3	180 (A_g)				
4	190 (A_g)	3	189	4	189
5	224 (B_g)	4	222	5	222
		5	270		266 ^{tetra}
6	313 (B_g)	6	305	6	306
7	317 (A_g)			7	315 ^{ambig}
8	330 (B_g)	7	331	8	335
9	345 (A_g)	8	343	9	347
				10	355 ^{sugg}
10	381 (A_g)	9	376		
11	382 (B_g)	10	376	11	382
12	466 (A_g)	11	473	12	476
13	489 (B_g)	12	498	13	502
14	533 (B_g)	13	534	14	537
15	548 (A_g)	14	557	15	559
16	601 (B_g)	15	613	16	616
17	631 (A_g)	16	633	17	637
		17	705		
18	748 (B_g)	18	780		764 ^{2nd}

$$\epsilon_\lambda = \frac{4\pi e^2}{M_0 V \omega_\lambda^2} \tilde{Z}_\lambda^{*2} \quad (9)$$

is the contribution to the trace of the dielectric tensor coming from the mode λ , and the scalar mode effective charge \tilde{Z}_λ^* is defined via $\tilde{Z}_\lambda^{*2} = \sum_\alpha \tilde{Z}_{\lambda\alpha}^{*2}$.

Presented in Table VII are the scalar mode effective charges \tilde{Z}_λ^* and the corresponding contribution to the static dielectric response ϵ_λ for each IR-active mode. (Note that T_{1u} and E_u modes are three-fold and two-fold degenerate, respectively. The ϵ_λ vs. ω_λ for the monoclinic phase are also presented graphically in Fig. 4.) From Table VII or Fig. 4, we find that for the monoclinic phase the softest modes have small \tilde{Z}_λ^* values and hence do not contribute much intensity, while the modes with largest \tilde{Z}_λ^* are at significantly higher frequency ($\sim 319 \text{ cm}^{-1}$). This observation will be important for explaining the relative smallness of the dielectric tensor of the monoclinic phase, as discussed below.

When all the modes are summed over, we obtain the total lattice contribution to the static dielectric response (the second term of Eq. (6)). We find

TABLE VII. Mode frequency, scalar mode effective charge, and contribution to the trace of the dielectric tensor for each IR-active mode.

	Mode (cm ⁻¹)	\tilde{Z}_λ^*	ϵ_λ
Cubic	258 (T_{1u})	1.17	31.80
Tetragonal	154 (E_u)	1.03	34.29
	334 (A_{2u})	1.48	14.92
	437 (E_u)	1.35	7.27
Monoclinic	181 (A_u)	0.07	0.05
	224 (B_u)	0.84	4.97
	242 (A_u)	0.22	0.31
	253 (A_u)	0.86	4.10
	305 (B_u)	0.42	0.69
	319 (B_u)	1.72	10.33
	347 (A_u)	1.09	3.54
	355 (B_u)	1.51	6.43
	401 (A_u)	1.57	5.44
	414 (B_u)	1.27	3.37
	478 (A_u)	0.93	1.34
	483 (B_u)	1.16	2.07
	571 (A_u)	0.84	0.77
	634 (A_u)	0.06	0.00
	711 (B_u)	0.88	0.55

$$\epsilon_{\text{cubic}}^{\text{latt}} = \begin{pmatrix} 31.8 & 0 & 0 \\ 0 & 31.8 & 0 \\ 0 & 0 & 31.8 \end{pmatrix}$$

$$\epsilon_{\text{tetra}}^{\text{latt}} = \begin{pmatrix} 41.6 & 0 & 0 \\ 0 & 41.6 & 0 \\ 0 & 0 & 14.9 \end{pmatrix}$$

$$\epsilon_{\text{mono}}^{\text{latt}} = \begin{pmatrix} 16.7 & 0 & 0.98 \\ 0 & 15.6 & 0 \\ 0.98 & 0 & 11.7 \end{pmatrix}$$

The calculated dielectric tensors have the correct forms expected from the crystal point group: the cubic one is diagonal and isotropic, the tetragonal one is diagonal with $\epsilon_{xx} = \epsilon_{yy} \neq \epsilon_{zz}$, and the monoclinic one is only block-diagonal in y and xz subspaces. Our values are also in very good agreement with previous theoretical calculations for the cubic and tetragonal phases. Ref. 12 reports that $\epsilon^{\text{latt}} = 29.77$ for the cubic phase, within about 6% of our result. Ref. 12 also gives the two independent components of ϵ^{latt} in the tetragonal phase as 42.36 and 15.03, again in excellent agreement with our results, and showing the same enormous anisotropy.

To compare with experiment, we note that ϵ_∞ can be estimated from the index of refraction n , which has been reported experimentally to be about 2.16 ($n^2 = \epsilon_\infty = 4.67$),¹¹ 2.192 ($\epsilon_\infty = 4.805$),¹⁰ and 2.19 ($\epsilon_\infty = 4.80$)⁹ for the cubic, tetragonal and monoclinic ZrO₂ phases, respectively. Theoretical works have reported that the orientational average $\bar{\epsilon}_\infty = 5.75$ for cubic ZrO₂,⁸ and $\epsilon_\infty^\parallel = 5.28$ and $\epsilon_\infty^\perp = 5.74$ ($\bar{\epsilon}_\infty = 5.59$) for tetragonal

ZrO₂.¹² We can see that ϵ_∞ does not vary strongly with structural phase, nor is there any evidence for strong anisotropy. Moreover, the only experimental measurements of ϵ_0 of which we are aware are on polycrystalline samples, for which we need to take an orientational average anyway. Therefore, we somewhat arbitrarily assume an isotropic value of $\epsilon_\infty = 5.0$ for the purposes of comparison with the total dielectric response. Then we obtain orientationally averaged static dielectric constants of 36.8, 46.6 and 19.7 for the cubic, tetragonal and monoclinic ZrO₂ phases, respectively.

Experimental reports of the value of ϵ_0 for monoclinic ZrO₂ span a wide range from about 16 to 25;^{9,41} our estimated value of 19.7 falls comfortably in the middle of this range. Unfortunately, we are not aware of any experimental measurements of the static dielectric response in the cubic or tetragonal phase. Since these phases exist only at elevated temperatures, comparison with zero-temperature theory would need to be made with caution in any case. However, neither the cubic-tetragonal nor the tetragonal-monoclinic transition is ferroelectric in character, so the influence of the thermal fluctuations on ϵ_0 is probably not drastic.

E. Discussion

As indicated in the Introduction, much current interest in ZrO₂ and related oxides is driven by the search for high- ϵ_0 materials for use as the gate dielectric in future-generation integrated-circuit devices. While the dielectric constant of monoclinic ZrO₂ is much bigger than that of SiO₂, our results indicate that it is actually rather low compared to the values in the range 35-50 expected for the tetragonal and cubic phases. From this perspective, it appears that monoclinic ZrO₂ has a disappointingly low static dielectric response.

As can be seen from Eq. (6) or (9), the contribution of a given mode to the dielectric response scales as $\tilde{Z}_\lambda^{*2}/\omega_\lambda^2$, so that a large ϵ_0 will result if there are modes that have simultaneously a large \tilde{Z}^* and a small ω . As can be seen from Table VII, this is not the case for monoclinic ZrO₂. Instead, we find that the cluster of modes with the lowest frequencies (< 250 cm⁻¹) also have low \tilde{Z}^* values (< 0.5), while the most active modes reside at higher frequencies ($\sim 300 - 500$ cm⁻¹). This is in direct contrast to the case of the cubic perovskite CaTiO₃ studied recently by Cockayne and Burton,⁴² who find a very soft mode ($\omega \simeq 100$ cm⁻¹) and very active ($\tilde{Z}^* \simeq 3$ mode, contributing to an enormous dielectric constant $\epsilon_0 > 250$).

The much larger values of ϵ_0 obtained for the cubic and tetragonal phases suggests that the unfavorable coincidence of low- ω and low- \tilde{Z}^* values may be peculiar to the monoclinic phase, and that other structural modifications (e.g., quasi-amorphous structures) may actually have a significantly larger ϵ_0 . This clearly presents an avenue for future study.

Finally, in low-symmetry structures such as the monoclinic (or especially amorphous) phases, it is of interest to attempt to decompose ϵ_0 spatially into contributions coming from different atoms in the structure. For example, one might ask whether it is primarily the three-fold or the four-fold oxygens that are responsible for the dielectric response in the monoclinic phase. For this purpose, we first carry out a decomposition $\epsilon_{\alpha\beta}^{\text{latt}} = \sum_{ij} \tilde{\epsilon}_{\alpha\beta}^{ij}$ of the lattice dielectric tensor into contributions

$$\tilde{\epsilon}_{\alpha\beta}^{ij} = \frac{4\pi e^2}{V} \sum_{\lambda} \frac{1}{\kappa_{\lambda}} R_{\alpha i}^{\lambda} R_{\beta j}^{\lambda}$$

arising from pairs of atoms, where κ_{λ} and $e_{j\beta}^{\lambda}$ are the eigenvalue and eigenvector of the force constant matrix $\Phi_{ij}^{\alpha\beta}$ for the phonon mode λ , V is the volume of unit cell, and $R_{\alpha j}^{\lambda} = \sum_{\beta} Z_{j,\alpha\beta}^* e_{j\beta}^{\lambda}$. We then heuristically define the contribution coming from atom i to be

$$\bar{\epsilon}_{\alpha\beta}^{(i)} = \sum_j \frac{1}{2} \left(\tilde{\epsilon}_{\alpha\beta}^{ij} + \tilde{\epsilon}_{\alpha\beta}^{ji} \right). \quad (10)$$

This atom-by-atom decomposition attributes most of the contribution to ϵ_0 as coming from the Zr atoms (exactly 2/3 in the cubic phase and close to this ratio in the other two phases). As for the oxygen, we found that both the three-fold and four-fold oxygen atoms make a similar contribution to the orientationally averaged dielectric constant in the monoclinic phase. (Not surprisingly, the anisotropies of the two oxygen contributions are somewhat different.) While this analysis has not proven especially fruitful here, it may be useful in future studies of low-symmetry (e.g., amorphous) phases.

IV. CONCLUSION

In summary, we have investigated here the Born effective charge tensors, lattice dynamics, and the contributions of the lattice modes to the dielectric properties of the three ZrO₂ phases. The structural parameters, including all internal degrees of freedom of the three ZrO₂ phases, are relaxed, and excellent agreement is achieved with experimental structural refinements and with previous *ab initio* calculations. The observed relative stability of the ZrO₂ phases is reproduced in our calculation. The calculated Born effective charge tensors show anomalously large values of Z^* , reflecting a strong dynamic charge transfer as the bond length varies and indicating a partially covalent nature of the Zr–O bonds. The calculated zone-center phonon mode frequencies are in good agreement with infrared and Raman experiments.

Finally, the lattice contributions to the dielectric tensors have been obtained. We find that the cubic and tetragonal phases have a much larger static dielectric response than the monoclinic phase, with an especially strong anisotropy in the tetragonal structure. The relatively low ϵ_0 in monoclinic ZrO₂ arises because the

few lowest-frequency IR-active modes happen to have rather small oscillator strengths, while the modes with the strongest dynamical mode effective charges occur at higher frequency. This result, together with the predicted increase of ϵ_0 in the cubic and tetragonal phases, suggests that the static dielectric constant is a strong function of the structural arrangement. Thus, there may be a prospect for larger ϵ_0 values in structurally modified (e.g., amorphous) forms of ZrO₂, or in solid solutions of ZrO₂ with other oxides.

ACKNOWLEDGMENTS

This work was supported by NSF Grant 4-21887. We would like to thank E. Garfunkel for useful discussions. One of us (X.Z.) thanks I. Souza for helpful discussions in connection with the calculation of Born effective charge tensors.

-
- ¹ L.C. Feldman, E. P. Gusev, and E. Garfunkel, *Ultrathin Dielectrics in Silicon Microelectronics*.
 - ² D. A. Buchanan and S. H. Lo, *Microelectronic Engineering* **36**, 13 (1997).
 - ³ G. Heiser and A. Schenk, *J. Appl. Phys.* **81**, 7900 (1997).
 - ⁴ H. S. Momose, M. Ono, T. Yoshitomi, T. Ohguro, S. I. Nakamura, M. Saito, and H. Iwai, *IEEE Trans. Electron Devices* **43**, 1233 (1996).
 - ⁵ G. B. Alers, D. J. Werder, Y. Chabal, H. C. Lu, E. P. Gusev, E. Garfunkel, T. Gustafsson, and R. S. Urdahl, *Appl. Phys. Lett.* **73**, 1517 (1998).
 - ⁶ J. V. Grahn, P. E. Hellberg, and E. Olsson, *J. Appl. Phys.* **84**, 1632 (1998).
 - ⁷ G. D. Wilk, R. M. Wallace, and J. M. Anthony, *J. Appl. Phys.* **87**, 484 (2000).
 - ⁸ F. Detraux, Ph. Ghosez, and X. Gonze, *Phys. Rev. Lett.* **81**, 3297 (1998).
 - ⁹ A. Feinberg and C. H. Perry, *J. Phys. Chem. Solids* **42**, 513 (1981).
 - ¹⁰ R. H. French, S. J. Glass, F. S. Ohuchi, Y. N. Xu, and W. Y. Ching, *Phys. Rev. B* **49**, 5133 (1994).
 - ¹¹ D. L. Wood and K. Nassau, *Appl. Opt.* **12**, 2978 (1982).
 - ¹² G.-M. Rignanese, F. Detraux, X. Gonze, and A. Pasquarello, *Phys. Rev. B* (in press).
 - ¹³ E. V. Stefanovich, A. L. Shluger, and C. R. A. Catlow, *Phys. Rev. B* **49**, 11560 (1994).
 - ¹⁴ M. Wilson, U. Schonberger, and M. W. Finnis, *Phys. Rev. B* **54**, 9147 (1996).
 - ¹⁵ J. K. Dewhurst and J. E. Lowther, *Phys. Rev. B* **57**, 741 (1998).
 - ¹⁶ B. Králik, E. K. Chang, and S. G. Louie, *Phys. Rev. B* **57**, 7027 (1998).
 - ¹⁷ G. Jomard, T. Petit, A. Pasturel, L. Magaud, G. Kresse, and J. Hafner, *Phys. Rev. B* **59**, 4044 (1999).

- ¹⁸ G. Stapper, M. Bernasconi, N. Nicoloso, and M. Parrinello, Phys. Rev. B **59**, 797 (1999).
- ¹⁹ S. Fabris, A. T. Paxton, and M. W. Finnis, Phys. Rev. B **61**, 6617 (2000).
- ²⁰ H. J. F. Jansen, Phys. Rev. B **43**, 7267 (1991).
- ²¹ C. J. Howard, R. J. Hill, and B. E. Reichert, Acta Crystallogr. Sect. B **44**, 116 (1988).
- ²² P. Aldebert and J. P. Traverse, J. Am. Ceram. Soc. **68**, 34 (1985).
- ²³ R. D. King-Smith and D. Vanderbilt, Phys. Rev. B **47**, 1651 (1993).
- ²⁴ E. Anastassakis, B. Papanicolaou, and I. M. Asher, J. Phys. Chem. Solids **36**, 667 (1975).
- ²⁵ T. Hirata, Phys. Rev. B **50**, 2874 (1994).
- ²⁶ C. Carlone, Phys. Rev. B **45**, 2079 (1992).
- ²⁷ H. Zhang, Y. Liu, K. Zhu, G. Siu, Y. Xiong, and C. Xiong, J. Phys. Cond. Matter **11**, 2035 (1999).
- ²⁸ D. M. Ceperley and B. J. Alder, Phys. Rev. Lett. **45**, 566 (1980).
- ²⁹ We used LDA but not GGA in this work for two reasons. First, we wanted to facilitate comparison with previous DFT studies on ZrO₂ that were carried out using LDA. Second, Ref. 17 has tested the effect of LDA and GGA's (PW91 and PB) on ZrO₂. These authors find that while the lattice parameters increase slightly with the use of the GGA (*a* is augmented less than 1% for the monoclinic ZrO₂), the *b/a* and *c/a* ratios and internal structural parameters are almost unaffected.
- ³⁰ D. Vanderbilt, Phys. Rev. B **41**, 7892 (1990).
- ³¹ H. J. Monkhorst and J. D. Pack, Phys. Rev. B **13**, 5188 (1976).
- ³² D. K. Smith and H. W. Newkirk, Acta. Crystallogr. **18**, 983 (1965).
- ³³ R. Ackermann, E. G. Rauh, and C. A. Alexander, High. Temp. Sci. **7**, 304 (1975).
- ³⁴ R. Resta, M. Posternak, and A. Baldereschi, Phys. Rev. Lett. **70**, 1010 (1993).
- ³⁵ W. Zhong, R. D. King-Smith, and D. Vanderbilt, Phys. Rev. Lett. **72**, 3618 (1994).
- ³⁶ P. Bouvier, H. C. Gupta, and G. Lucazeau, J. Phys. Chem. Solids **62**, 873 (2001).
- ³⁷ A. P. Mirgorodsky, M. B. Smirnov, and P. E. Quintard, J. Phys. Chem. Solids **60**, 985 (1997).
- ³⁸ T. Hirata, E. Asari, and M. Kitajima, J. Solid State Chem. **110**, 201 (1994).
- ³⁹ C. Pecharromán, M. Ocaña, and C. J. Serna, J. Appl. Phys. **80**, 3479 (1996).
- ⁴⁰ All three ZrO₂ phases are non-piezoelectric, so the fixed-strain and free-stress dielectric tensors are identical for these systems.
- ⁴¹ G.-M. Rignanese, X. Gonze, and A. Pasquarello, Phys. Rev. B **63**, 104305 (2001).
- ⁴² E. Cockayne and B. P. Burton, Phys. Rev. B **62**, 3735 (2000).